Intraband absorption and Stark effect in silicon nanocrystals

J. S. de Sousa,[1] J.-P. Leburton,[2] V. N. Freire,[1] and E. F. da Silva, Jr.[3]
[1]*Departamento de Física, Universidade Federal do Ceará, Caixa Postal 6030, 60455-760 Fortaleza, Ceará, Brazil*
[2]*University of Illinois at Urbana-Champaign 405 North Mathews Avenue, Urbana, Illinois 61801, USA*
[3]*Departamento de Física, Universidade Federal de Pernambuco, 50670-901 Recife, Pernambuco, Brazil*
(Received 3 May 2005; published 27 October 2005)

A theoretical investigation of the combined effect of confinement geometry, valley degeneracy, crystallographic orientations, and anisotropy of the effective mass on the intraband absorption of the conduction band of Si nanocrystals is presented. We show that the coupling between the nanocrystal shape and arbitrary orientations of the crystalline Si core plays a dramatic role in the intraband optical properties through interesting changes in the electronic structure and intra- and inter-valley degeneracy. Different orientations of the crystalline Si also affect the shape and orientation of the orbital wave functions, thereby modifying transition rules and fine structure of the intraband absorption. The anisotropy of the effective mass is also responsible for the emergence of absorption peaks that are not present in isotropic nanocrystals. Additional intraband transitions are also induced by changes in the nanocrystal shape with respect to spherical dots. Moreover, the quantum confined Stark effect blueshifts the absorption peaks and induces the appearance of peak structures as a consequence of the relaxation of selection rules caused by the displacement of the wave functions in response to external electric fields. This effect was found to be only appreciable in large nanocrystals.

DOI: 10.1103/PhysRevB.72.155438 PACS number(s): 73.21.La, 73.22.Dj, 78.67.Bf, 78.20.Bh

I. INTRODUCTION

With recent advances in materials manipulation at the nanoscale, the degrees of freedom of charge carriers can be controlled to produce electron confinement along the three dimensions of space. From the point of view of quantum confinement, engineering the electronic structure of materials by means of shape and size control offers the possibility of tailoring the energy spectrum to produce desirable intra- and inter-band optical transitions. These features are useful for the development of optoelectronic devices with tunable emission or transmission properties and ultra-narrow spectral linewidths. In this context, the development of Si based optoelectronics is one of the most pursued technologies, because of its full compatibility with Si microelectronics. Hence, it is well known that despite the Si indirect band gap, the optical and electronic properties of Si layers are rather different from their bulk counterpart when they are reduced to nanometer dimensions for which the band gap becomes direct due to the folding of the band structure in the Brillouin zone.[1,2] For example, (0D–2D) Si/SiO_2 nanostructures exhibits visible and efficient photoluminescence at room temperature.[3] In addition, the recent demonstration of optical gain in Si/SiO_2 nanocrystals (NC's) (Ref. 4) and high-speed Si optical modulator based on metal-oxide-semiconductor capacitor (MOS) (Ref. 5) undoubtedly opened the path for the development of Si-based photonics.

Recently, intraband absorption in the midinfrared spectral range has been demonstrated in Ge/Si self-assembled NC's. This absorption is in-plane polarized and corresponds to transitions from the ground state of the dots to the continuum states.[6] It was also predicted by tight-binding calculations that zero- and one-phonon intraband transitions in Si NC's present unusual properties and high efficiency compared to III-V NC's.[7] This fact indicates that Si/SiO_2 NC's might be an alternative to the development of infrared photodetectors (IP's) that is compatible with standard Si technology.

NC formation is sensitive to intrinsic variations in shape, size, and crystallographic orientations. Hence, the possibility of building NC's in different shapes has been already demonstrated,[8,9] and size distribution can be estimated.[10] In addition, during the synthesis of Si NC's in SiO_2, NC's with different crystallographic directions may form in the same sample. Consequently, the anisotropy and degenerated nature of the Si band structure combined with various geometrical effects strongly influence the quantum mechanical properties of Si NC's. Recently, it was shown that the tunneling time of single electrons into NC's in nonvolatile flash memories is affected by their crystal orientation.[11]

This work aims at the investigation of the interplay among confinement geometry, valley degeneracy, crystallographic orientations, and anisotropy of the effective mass on the intraband optical properties of the conduction band of Si NC's. In addition, we study the influence of the Stark effect on the intraband transitions because of its potential application in infrared detection and emission. In Sec. II, models for the electronic structure and optical properties are described. The electronic structure calculation is obtained within the effective mass framework and takes into account the multivalley and anisotropy of Si band structure, while the intraband absorption model relies on the Fermi's golden rule. Section III is dedicated to the discussion of the results, divided into two subsections: (i) the role of shape, crystallographic orientations, and size dependence on the electronic structure of Si NCs, and (ii) the consequences of such parameters on the intraband optical properties. Finally, some final remarks are drawn in Sec. IV.

II. PHYSICAL MODEL

A. Model structure

Scanning probe microscopy measurements of samples grown by different methods indicate that actual Si NC's are

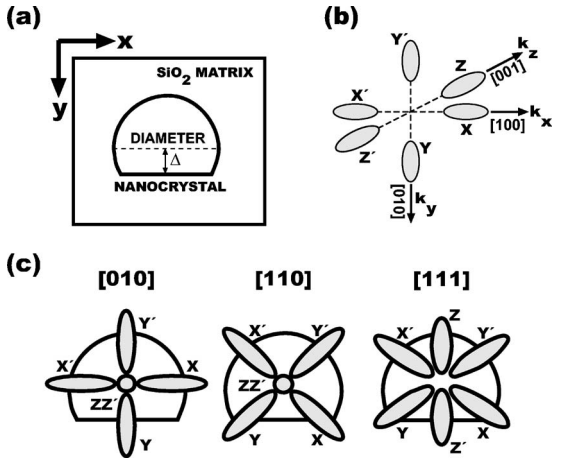

FIG. 1. (a) Schematics of the simulation cell studied in this work. We define a truncation parameter Δ which controls the NC shape, which is (i) spherical for $\Delta=D/2$ (D represents the NC diameter), (ii) hemispherical for $\Delta=0$ and (iii) truncated for intermediate values. (b) Sixfold Si band energy valleys. (c) Top view (xy plane) of the orientation of the Si energy valleys with respect to truncation of the NC for [010], [110], and [111] crystallographic planes of the Si bulk perpendicular to the y direction of the simulation cell.

similar to truncated spheres.[8,12] Therefore, for a realistic calculation, we introduce flat truncations perpendicular to the y direction in spherical NC's by means of a truncation parameter Δ, which controls the NC shape, as shown in Fig. 1(a).

The Si band structure has six anisotropic and degenerated energy valleys in the [100] equivalent directions, where each doubly degenerated energy valleys are labeled as XX', YY', and ZZ', as depicted in Fig. 1(b). In a recent paper, Thean and Leburton demonstrated that the alignment of such k-space directions with the main axes of the simulation cell leads to interesting effects on the electronic structure, which was attributed to the coupling of the anisotropic effective mass with the NC shape.[13] Here, we generalize their model to deal with any alignment of the Si crystalline structure with respect to the NC shape, and discuss some particular cases, namely, [110] and [111] directions perpendicular to the NC truncation plane. As a consequence of different crystalline orientations, the configuration of the energy valleys with respect to the NC geometry are modified. While this modification is not so important in NC's formed by single valley isotropic semiconductors, we demonstrate it rules the electronic structure and optical absorption of Si NC's. Figure 1(c) depicts a schematics of the energy valleys configuration with respect to a truncated Si NC for the [010], [110], and [111] crystalline orientations. In order to take into account such effects within an effective mass based model, the electronic states $\Psi_{v,j}(\mathbf{r})$ are obtained by solving the three-dimensional Schrodinger equation written in the following form:

$$\frac{\hbar^2}{2}[\nabla^T M_v^{-1}(\mathbf{r})\,\nabla + V(\mathbf{r})]\Psi_{v,j}(\mathbf{r}) = E_{v,j}\Psi_{v,j}(\mathbf{r}) \tag{1}$$

where $v=(XX',YY',ZZ')$ indicates the energy valleys set and j represents the state index. The differential operator ∇^T, the position-dependent effective mass $M_v^{-1}(\mathbf{r})$, and the confinement potential $V(\mathbf{r})$ are, respectively, given by

$$\nabla^T = \frac{\hbar}{i}(\partial_x \partial_y \partial_z), \tag{2}$$

$$M_v^{-1}(\mathbf{r}) = \hat{\sigma}\begin{pmatrix} m_1^{-1}(\mathbf{r}) & 0 & 0 \\ 0 & m_2^{-1}(\mathbf{r}) & 0 \\ 0 & 0 & m_3^{-1}(\mathbf{r}) \end{pmatrix}\hat{\sigma}^T, \tag{3}$$

$$V(\mathbf{r}) = \Delta E_C(\mathbf{r}) - e\mathbf{F}_{\mathrm{EXT}}\cdot\mathbf{r}, \tag{4}$$

where $\Delta E_C(\mathbf{r})$ represents the conduction band discontinuity between Si and SiO_2, whose value is 3.2 eV. Here, we assume the NC is placed in a constant and uniform electric field $\mathbf{F}_{\mathrm{EXT}}$. Equation (1) must be solved for each pair of degenerated energy valleys $v=XX',YY',ZZ'$, which are represented by the following mass configurations: (i) $m_1=m_l$, $m_2=m_3=m_t$; (ii) $m_2=m_l$, $m_1=m_3=m_t$; (iii) $m_1=m_2=m_t$, $m_3=m_l$, respectively, where $m_l=0.916$ and $m_t=0.190$. $\hat{\sigma}$is a unitary and invertible rotation operator which is responsible to reproduce the configuration of the Si energy valleys with respect to the NC for a given crystalline orientation. Therefore, in order to obtain the k-space directions [010], [110], and [111] pointing to the positive y direction of the unit cell, $\hat{\sigma}$ assumes the following forms:

$$\hat{\sigma}_{[010]} = I, \tag{5}$$

$$\hat{\sigma}_{[110]} = R_z(\pi/2), \tag{6}$$

$$\hat{\sigma}_{[111]} = R_x(\pi/2)R_z(\pi/2), \tag{7}$$

Here, I represents an identity matrix and $R_i(\theta)$ $(i=x,y,z)$ is a matrix operator representing a rotation by θ around the i direction, which are given by

$$R_x(\theta) = \begin{pmatrix} 1 & 0 & 0 \\ 0 & \cos\theta & \sin\theta \\ 0 & -\sin\theta & \cos\theta \end{pmatrix},$$

$$R_y(\theta) = \begin{pmatrix} \cos\theta & 0 & -\sin\theta \\ 0 & 1 & 0 \\ \sin\theta & 0 & \cos\theta \end{pmatrix}, \tag{8}$$

$$R_z(\theta) = \begin{pmatrix} \cos\theta & \sin\theta & 0 \\ -\sin\theta & \cos\theta & 0 \\ 0 & 0 & 1 \end{pmatrix}.$$

B. Intraband optical properties

The optical absorption calculation is based on the Fermi's golden rule, for which the intraband absorption coefficient is given by[14]

$$\alpha(\hbar\omega) = \frac{2\pi\hbar\omega}{\Omega nc\epsilon_0} \sum_{v,l,u} |\hat{e}\cdot\mu_{ul}|^2 A(\hbar\omega)(n_l - n_u), \qquad (9)$$

where the index v stands for the energy valleys, the subscripts l,u indicate the lower (initial) and upper (final) transition states, respectively. The quantities Ω, n, and c are the NC volume, index of refraction, and speed of light, respectively. $\mu_{ul}=q\langle\Psi_u|\mathbf{r}|\Psi_l\rangle$ is the electric dipole moment of the transition from l state to u state, $A(\hbar\omega)$ is a line broadening Lorentzian function for which the mean width at half maximum (MWHM) was arbitrarily chosen as 30 meV. $n_{u,l}$ represent the upper and lower states occupation factor. For an accurate calculation of these quantities, Gibbs statistics should be used for high temperatures. However, due to the low dimensionality of NC's, the energy states are well separated ($\Delta E > k_B T$) such that thermal occupation is negligible. Therefore, $n_{u,l}$ assume the integer values 0, 1, and 2 (individual spins are neglected). Particularly, we set $n=1$ for the ground state of each pair of valleys and $n=0$ for all upper states. In addition, the study on the optical transitions by means of the dimensionless oscillator strength f_{ul} can offer additional information on the fine structure and selection rules of the optical absorption. This quantity is given by

$$f_{ul} = \frac{2m_0(E_u - E_l)}{\hbar^2} |\langle\Psi_u|\mathbf{r}|\Psi_l\rangle|^2, \qquad (10)$$

where m_0 is the electron mass in vacuum (here we disregard anisotropy), and $(E_u - E_l)$ is the transition energy from l state to u state.

C. Numerical methods

The calculation of the electronic structure is performed through the discretization of Eq. (1) by means of a finite-difference scheme on a tridimensional rectangular mesh with $n_x n_y n_z$ points. The matrix resulting from this stage are sparse and diagonal, where the number of diagonal changes according to the crystalline orientation. For example, the simplest [010] case exhibits seven diagonals, while more complex orientations may reach 19 bands ([111] crystal orientation) because the transformed effective mass tensor $M_v^{-1}(\mathbf{r})$ in Eq. (1) is no longer diagonal, and the additional matrix elements contribute with the cross derivatives $\partial_m M^{-1}_{v(mn)}(\mathbf{r})\partial_n\Psi(\mathbf{r})$ to the discretization step. There are several computational methods to extract the eigenvalues and eigenfunctions from sparse banded matrices,[15,16] and for an arbitrary chosen number of states, the implicitly restarted block Arnoldi method is the best available.[17]

III. RESULTS

A. Shape, crystallographic orientation, and size dependence

In Fig. 2, the size dependence of the lowest four bound states of a spherical NC shape is shown. Because of the spherical symmetry of confinement, the electron states in the six equivalent valleys are degenerated. This degeneracy also holds for different alignments of the crystallographic orientation. In this case, the degenerated states only differ by a rotation of the wave functions by the same transformation of NC crystalline orientation, as shown in the inset of Fig. 2.

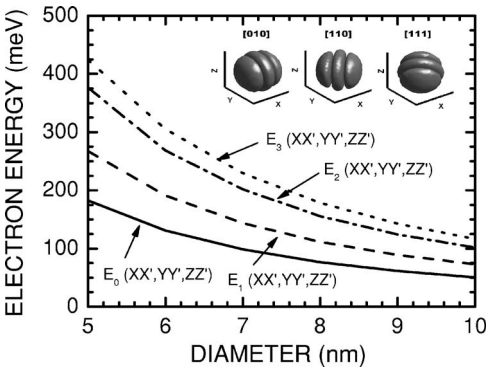

FIG. 2. Size dependence of the lowest four bound states of a spherical NC for the [010], [110], and [111] orientations perpendicular to the y direction of the simulation cell. The inset graph shows the wave functions of the $E_2(XX')$ state for three crystal orientations.

The degeneracy of the energy valleys is broken with the inclusion of truncations in the NC due to the anisotropic effective mass, as shown by Thean and Leburton for the [010] orientation.[13] Figure 3 shows the dependence of energy states on the truncation parameter Δ, which controls the NC shape [see Fig. 1(b)], for a NC with 10 nm of diameter and [010] crystal orientation along the truncation direction. For this particular case, XX' and ZZ' energy states are degenerated for truncated NC's, and the NC ground state belongs to the YY' valley. This sounds paradoxal because of the stronger confinement in the y direction. However, the effective mass in this direction is $m_l(>m_t)$, which decreases the kinetic energy, and causes the NC ground state to be at the YY' valley. For the upper states, more complex rules apply. In the case of other crystalline orientations, the energy states and valley degeneracy change due to a different coupling of the effective mass tensor with the confining potential. This is shown in Table I for a truncated NC with 10 nm of diameter ($\Delta=2.5$ nm). In the case of [110] orientation, this transformation represents a rotation of 45° of the effective mass

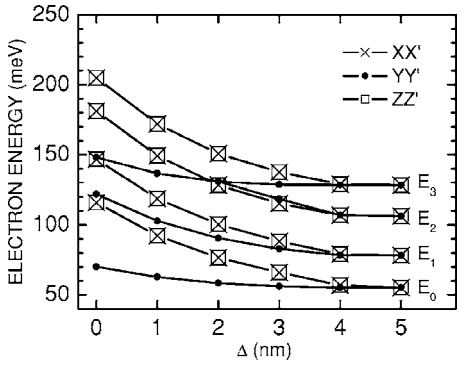

FIG. 3. Dependence of the lowest four electron states (E_j, where $j=0,\ldots,3$) on the truncation parameter Δ of a 10 nm wide NC [010] crystal orientation. The energy states within the XX', YY', and ZZ' valleys are represented by the symbols ×, •, and □, respectively.

TABLE I. Lowest four electron states (in meV) in each energy valley of a 10 nm wide truncated NC ($\Delta=2.5$ nm). The energy valleys degeneracy is displayed in bold face.

		XX'(meV)	YY'(meV)	ZZ'(meV)
[010]	E_0	**63.1902**	53.6738	**63.1902**
	E_1	**85.3842**	85.5496	**85.3842**
	E_2	**113.5710**	119.6967	**113.5710**
	E_3	**128.8813**	119.6967	**128.8813**
[110]	E_0	**57.3035**	**57.3035**	63.1902
	E_1	**86.5648**	**86.5648**	85.3842
	E_2	**122.8637**	**122.8637**	113.5710
	E_3	**123.1737**	**123.1737**	128.8813
[111]	E_0	**58.9511**	**58.9511**	**58.9511**
	E_1	**86.2104**	**86.2104**	**86.2104**
	E_2	**120.8261**	**120.8261**	**120.8261**
	E_3	**124.4137**	**124.4137**	**124.4137**

tensor around the z axis that mixes the XX' and YY' energy valleys, creating degeneracy between these valleys. As the ZZ' valley is unchanged, their energy states remain the same as in the [010] case. As for the [111] crystal orientation, an equal mixing of the energy valleys with respect to the confining potential induces full degeneracy among them, independently of the nonspherical shape.

An overview of degeneracy and size dependence of the NC's states is shown in Fig. 4 for a hemispherical NC ($\Delta=0$ nm) as a function of NC diameter. The [010] case exhibits the smaller degree of degeneracy. Above $E_0(XX',ZZ')$ states, we observe a bunching of states, for which the adjacent energy separation is nearly k_BT at room temperature even for small NC dimensions. For the [110] orientation, the lowest 12 NC states are separated in three clusters, in which the energy separation is smaller than k_BT. In the [111] case, these states group into three sets of degenerated states. The only difference for the spherical NC is that E_2 and E_3 states of each energy valley become degenerated for this shape, differently from nonspherical NC's. We remark that changes in the energy states and wave functions induced by the interplay of confinement potential and anisotropy of the effective mass will interfere in the transition rules and optical properties of Si NC's, as we shall see below.

B. Intraband absorption

The schematics of intraband transitions in the conduction band of Si NC's is depicted in Fig. 5. We simulate the condition where only six electrons are present in the NC's and assume all of them have thermalized down to the ground state with one electron per energy valley; hence, the photon absorption takes place from these states to the upper empty ones. Due to the computational cost, only 20 confined states are computed for each pair of valleys, totalizing 57 possible transitions.

Figure 6 depicts the absorption coefficient for spherical NC's with 3, 5, and 10 nm diameters, respectively. All absorption coefficients exhibit two peaks (a very weak and a strong one), which appears to be a general feature of Si/SiO_2 spherical NC's. The expected blueshift of the peaks and their separation are inversely proportional to the square of the NC diameter, which is in agreement with the relation between the energy level separation and the size of confinement L, i.e., $\Delta E_n \propto L^{-2}$. We must remark that this behavior is a characteristic of calculations based on the effective mass framework. The actual relationship between energy level separation is less than the inverse square of the NC size.[18] Due to

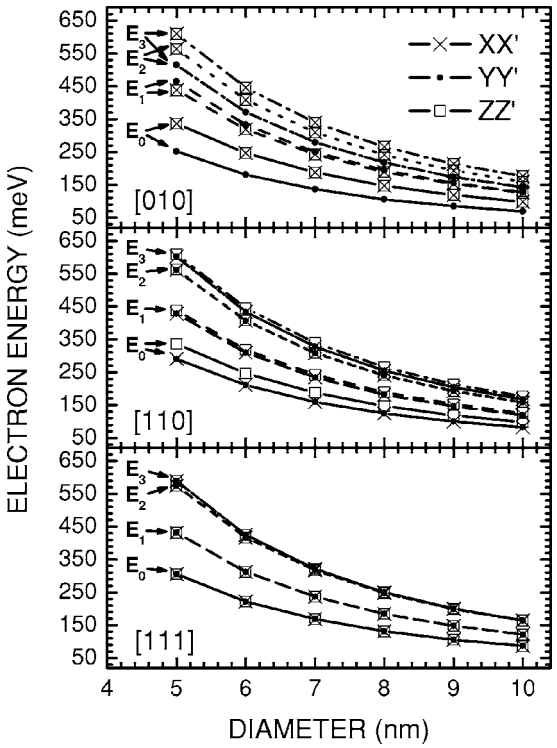

FIG. 4. Size dependence of the lowest four electron states (E_0-solid, E_1-dashed, E_2-dotted, and E_3-dash-dotted lines, respectively) in a hemispherical NC with [010], [110], and [111] crystallographic orientations.

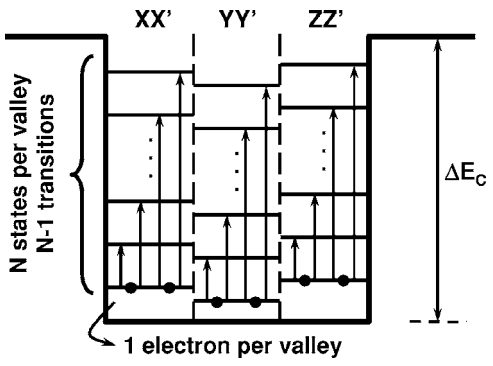

FIG. 5. Schematics of intravalley intraband transitions within the conduction band of Si NC's. Only the ground state of each valley is occupied (only one electron), and the transitions occur from this to the upper excited states. The possibility of intervalley transitions is disregarded. Due to the computational cost, we arbitrary chose $N=20$ in this work.

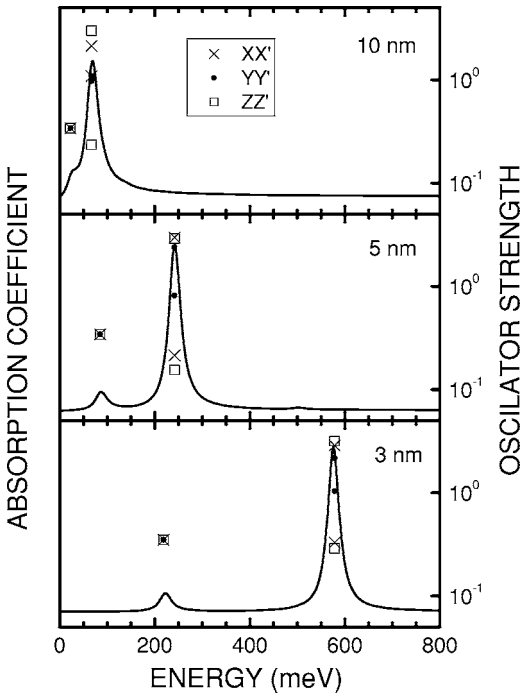

FIG. 6. (Left axis) Intraband absorption coefficient of spherical NC's with 3, 5, and 10 nm of diameter and [010] orientation of crystalline bulk. (Right axis) Oscillator strength of the most important transitions ($f_{ul} > 10^{-1}$) for each valley. Transitions within the XX', YY', and ZZ' valleys are represented by the symbols ×, •, and □, respectively.

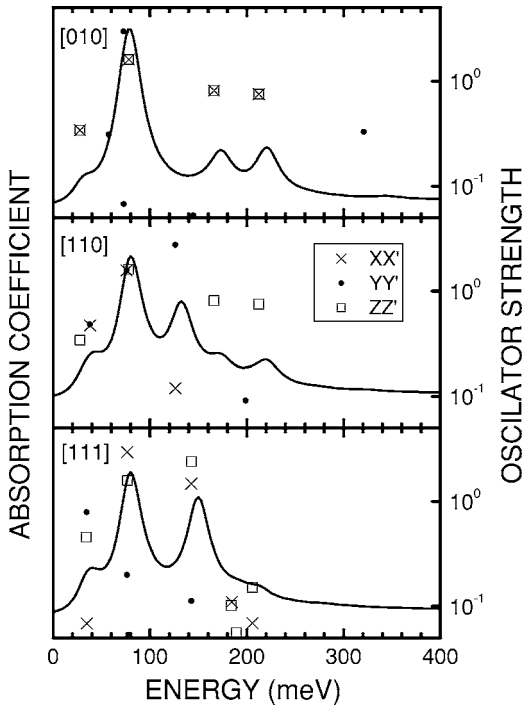

FIG. 7. (Left axis) Intraband absorption coefficient of a hemispherical NC with 10 nm of diameter for the [010], [110], and [111] orientations of crystalline bulk. (Right axis) Oscillator strength of the most important transitions ($>10^{-1}$) for each valley. Transitions within the XX', YY', and ZZ' valleys are represented the symbols ×, •, and □, respectively.

the high symmetry of spherical NC's, quantum states in XX', YY', and ZZ' valleys are degenerated, with the orientation of the wave functions in each valley, rotated by 90° from one another.[13] By labeling $n \rightarrow m$ a transition from the nth to the mth state, the first absorption (weakest) peak is due to $0 \rightarrow 1$ transitions, i.e., from the ground state to the first excited state, within all energy valleys. Due to the tridimensional orientation of the wave functions of the initial and final states, these transitions have all the same oscillator strengths. The second (strongest) peak is attributed to $0 \rightarrow (3,4)$ transitions, i.e., from the ground state to third and fourth excited states within each valley. We notice that the final states are degenerate (both transitions have the same energy) and the difference of parity between initial and final states makes the oscillator strengths for these transitions stronger than for the $0 \rightarrow 1$ transitions. Despite the degeneracy, the strongest peak is dominated by the $0 \rightarrow 4$ transition. We point out that the absence of peak structure at high energies for each NC diameter is due to the limitation on the number of calculated states. Moreover, for simplicity, we did not show transitions whose oscillator strengths are too weak to be seen in the absorption spectra ($f_{ul} < 10^{-1}$).

In Fig. 7, the absorption coefficient of a hemispherical NC with 10 nm of diameter is depicted for the [010], [110], and [111] crystalline orientations of bulk Si. As expected, the truncations break the spherical symmetry and induce transitions and absorption peaks, making the hemispherical NC's optically active in a broader energy range in comparison to the spherical case. Remarkably, the crystalline orientation strongly affects the absorption spectra. This is a consequence of the interplay between the effective mass tensor and the confinement shape that changes the energy spectrum and degeneracy among valleys. For NC's with [010] orientation along the truncation direction, XX' and ZZ' valleys become degenerated. We observe four main peaks, all related to transitions within XX' and ZZ' valleys, which are characterized by the same oscillator strength. These peaks originate from the following transitions: The first peak at 27.8 meV is a $0 \rightarrow 1$ transition while the peaks at 78.1, 166.3, and 212.4 meV are due to $0 \rightarrow 3$, $0 \rightarrow 8$, and $0 \rightarrow 12$ transitions, respectively. For the [110] orientation, the XX' and YY' valleys are degenerated. However, unlike the [010] case, the main absorption peaks are not necessarily generated by transitions within XX' and YY' valleys. Here, we identify five absorption peaks. The first peak at 38 meV is a $0 \rightarrow 1$ transition within XX' and YY' valleys. The second peak is a superposition of transitions at 75.9 and 78.1 meV, represented by the $0 \rightarrow 2$ (within XX' and YY' valleys) and $0 \rightarrow 3$ (within ZZ' valley) transitions, respectively. The third peak at 126.2 meV is due to $0 \rightarrow 5$ transitions in XX' and YY' valleys, and the last two peaks at 166.3 and 212.3 meV are caused by $0 \rightarrow 8$ and $0 \rightarrow 12$ transitions, respectively, both in the ZZ' valleys. For the [111] orientation, four absorption peaks are observed. The first one at 34.3 meV originates from $0 \rightarrow 1$ transitions in YY' and ZZ' valleys. The peaks near 76 meV are due to $0 \rightarrow 2$ (in XX' and YY' valleys) and $0 \rightarrow 3$ (in ZZ' valley) transitions. Finally, the last two peaks at 142.6 and 205.7 meV are caused by $0 \rightarrow 6$ (in all XX', YY', and ZZ'

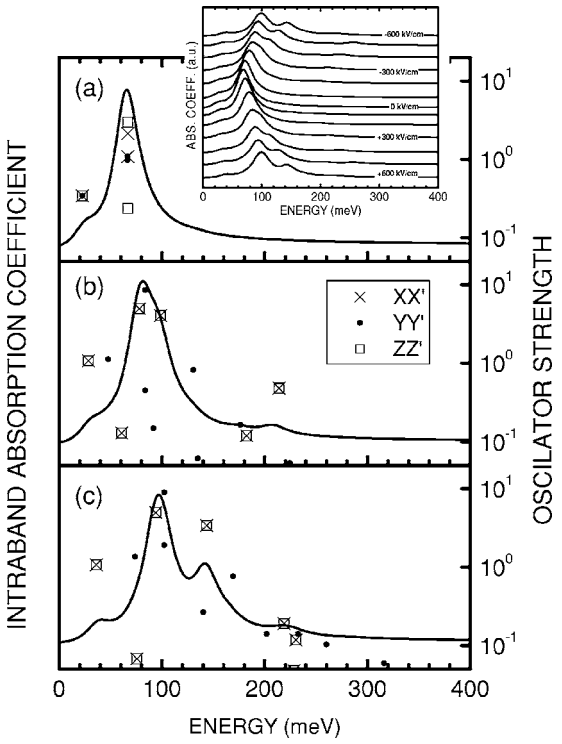

FIG. 8. Intraband absorption coefficient of a biased 10 nm wide spherical NC with the [010] crystallographic orientation for F_{EXT} pointing to positive y direction with intensities values of (a) 0 kV/cm, (b) 300 kV/cm, and (c) 600 kV/cm. In the inset graph, the intraband absorption is depicted for F_{EXT} varying from −600 to 600 kV/cm from top to bottom. (Right axis) Oscillator strength of the most important transitions ($>10^{-1}$) for each valley. Transitions within the XX', YY', and ZZ' valleys are represented the symbols ×, •, and □, respectively.

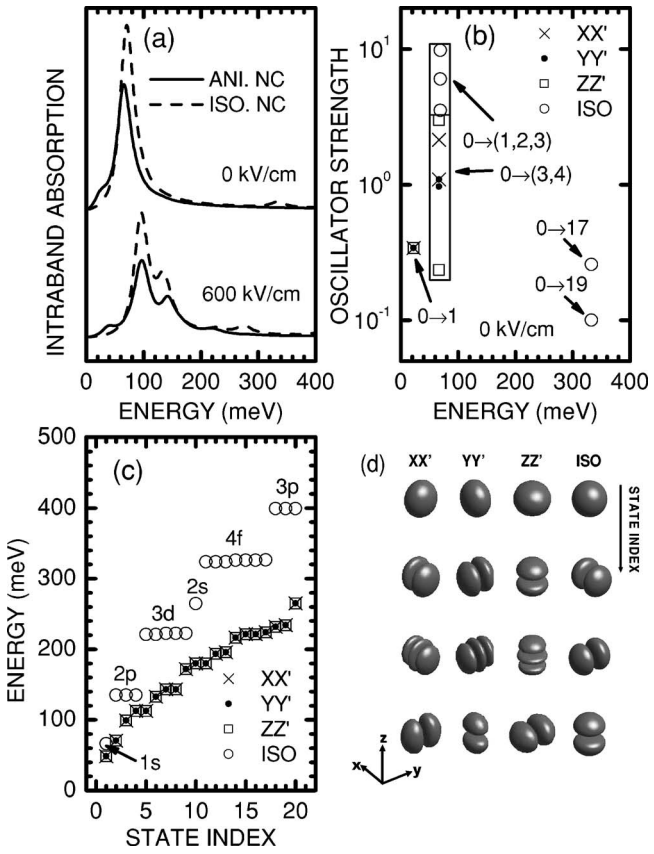

FIG. 9. Comparison between spherical NC's (10 nm of diameter) with isotropic (ISO) and anisotropic effective masses (XX', YY', and ZZ' valleys of a [010] oriented NC) for the following properties: (a) absorption coefficient with and without bias (600 kV/cm), (b) oscillator strengths at zero bias, (c) energy spectrum for the lowest 20 states, where the state indexes j are displayed in the horizontal axis, and (d) orbital wave functions of the lowest four confined states, where the state index j grows from top to bottom. The multivalley feature is not present in isotropic NC's.

valleys) and $0\rightarrow 10$ (only in ZZ' valley) transitions.

Figures 8(a)–8(c) show the absorption coefficient of a 10 nm wide spherical NC's with [010] crystal orientation under the influence of external biases of $F_{EXT}=0$, 300, 600 kV/cm parallel to the y direction. An overview of the influence of F_{EXT} on the intraband absorption of spherical NC's is shown in the inset graph of Fig. 8,where F_{EXT} varies from −600 to 600 kV/cm (from top to bottom). Due to the highly symmetrical NC shape, the absorption response is isotropic with respect to direction of F_{EXT} for a given magnitude. Moreover, different crystalline orientations do not change the position of the absorption peaks for spherical NC's. An expected general trend is the blueshift of the absorption peaks caused by the quantum confined Stark effect. However, the main peak of the unbiased case, attributed to transitions $0\rightarrow(3,4)$, splits in two. The first one is attributed to the $0\rightarrow 3$ (XX', YY', and ZZ' valleys) transitions, and the second peak to $0\rightarrow 6$ (XX' and ZZ' valleys) and $0\rightarrow 4$ (YY' valleys) transitions. Due to the coupling among F_{EXT}, anisotropic effective mass and confinement geometry, the $0\rightarrow 6$ transitions are forbidden for $F_{EXT}=0$, as well as the $0\rightarrow 4$ (XX' and ZZ' valleys) transitions for $F_{EXT}=600$ kV/cm. Therefore, the appearance of peak structures in biased NC's is attributed to the relaxation of selection rules caused by the displacement of the wave functions in response to F_{EXT}. We remark that this effect is also observed in NC's made of isotropic mass semiconductors. This is shown in Figs. 9(a) and 9(b), where the absorption spectra of 10 nm diameter spherical NC's with anisotropic mass (Si) on one hand, and with unrealistic isotropic effective mass taken to be m_t on the other hand, are compared for $F_{EXT}=0$, 600 kV/cm. The effective mass anisotropy has three major consequences on the NC energy spectrum in comparison to its isotropic counterpart: (i) The shape of orbital wave functions changes considerably, which (ii) creates a whole set of transition rules, and (iii) modification in the energy levels and intra- and intervalley degeneracy schemes. These changes are better visualized in Figs. 9(c) and 9(d), which compare the energy spectrum of isotropic and anisotropic NC's and their respective orbital wave functions, respectively. The isotropic effective mass leads to an electronic structure that is very similar to the hydrogen atom with s, p, d, and f-like orbitals and their respective degeneracies. On the other hand, a similar notation to label the energy states for anisotropic NC's is no longer possible.

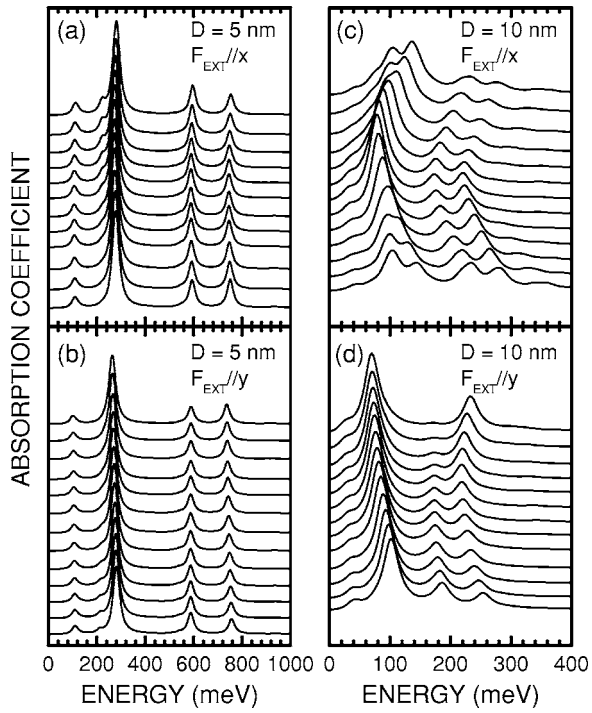

FIG. 10. Intraband absorption coefficient of a biased 5 nm (left column) and 10 nm (right column) wide hemispherical NC with the [010] crystallographic orientation for F_{EXT} varying from −600 to 600 kV/cm from top to bottom pointing to x (top row) and y (bottom row) directions.

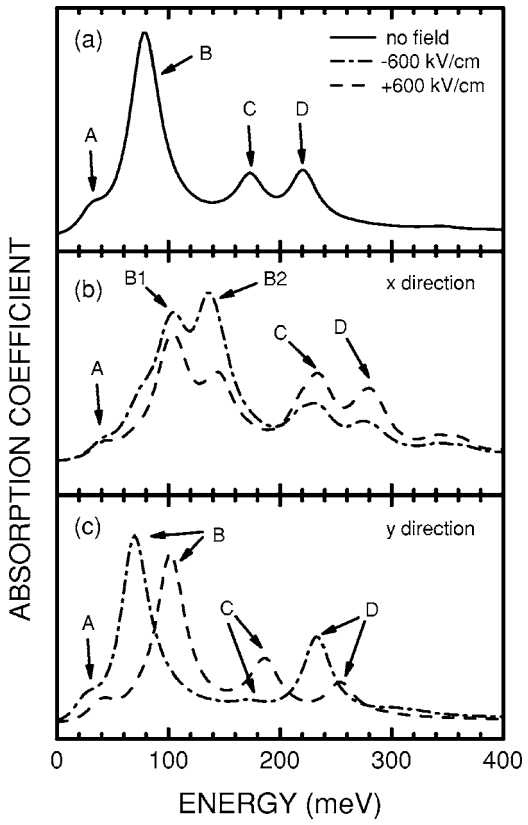

FIG. 11. Comparison of the intraband absorption coefficient of (a) unbiased and biased [panels (b) and (c)] hemispherical NC's with 10 nm of diameter and [010] crystal orientation. In this figure, only $F_{EXT}=\pm 600$ kV/cm pointing to both x and y directions are used.

In the case of biased hemispherical NC's, we notice that smaller NC's weakly respond to electric fields. These results are displayed in Fig. 10 for hemispherical NC's with diameters of 5 and 10 nm, and [010] crystalline orientation. This is caused by the strong confinement that restrains the displacement of the electron wave functions, and it is also observed in spherical NC's. However, the optical response is highly dependent on the magnitude and direction of F_{EXT} for larger nonspherical NC's. Because of the cylindrical symmetry of the NC shape with respect to the y axis, we expect the absorption spectra to be magnitude independent for $\pm F_{EXT}\|x$ (or $\pm F_{EXT}\|z$). Indeed, peak positions remain the same, but their intensities change for opposite directions of $F_{EXT}\|x$. As for $F_{EXT}\|y$, the absorption spectra exhibits a totally different behavior in comparison to $F_{EXT}\|x$ with respect to its direction. Concerning the fine structure of the absorption coefficient of hemispherical NC's, Fig. 11 displays the absorption spectra and the oscillator strengths for $F_{EXT}=-600$, 0, +600 kV/cm pointing to both x and y directions. As discussed previously, the unbiased [010] hemispherical NC exhibits four peaks, which are labeled as A, B, C, and D in Fig. 11(a). For $F_{EXT}\|x$, peaks A, C, and D are blueshifted nearly 10, 60, and 60 meV's, respectively, independently on the direction of $F_{EXT}\|x$. However, peak B splits in two (B1 and B2) as in the spherical NC. In the case of $F_{EXT}\|y$, all peaks are blueshifted and no splitting occurs, and their amplitudes depend on the direction of $F_{EXT}\|y$ because the wave functions have their displacement restrained to a smaller range in comparison to the x and z directions. This constraint affects the Stark shifts and the relative separation of the absorption peaks differently, whether the wave functions are squeezed against the flat truncation ($F_{EXT}\|y<0$) or the curved wall ($F_{EXT}\|y>0$). For positive values, the amplitude of the shifts are larger than for negative ones because the distance from the NC centroid to the curved wall is larger than to the flat truncation.

The analysis for other crystal orientations ([110] and [111]) is much more complicated, as shown in Fig. 12. Similar to the [010] case, $F_{EXT}\|y$ only shifts the absorption peaks, and its direction affects the amplitude of the Stark shifts due to the movement restrictions. However, the figure shows that the peaks positions are quite affected by the direction of $F_{EXT}\|x$, in contrast with the [010] case for which only the peak intensities change. This is attributed to a complicated coupling of the confinement geometry with effective mass tensor, which is no longer a diagonal matrix. This effect is not so strong for 7 nm wide NC's and almost invisible for very small NC's (3–5 nm).

IV. CONCLUDING REMARKS

In conclusion, we performed a theoretical study of the intraband transitions in Si NC's by using an effective mass based multivalley model. Our results show the shape of Si NC's strongly influences the absorption spectra by inducing variety of transitions. The coupling between the NC geom-

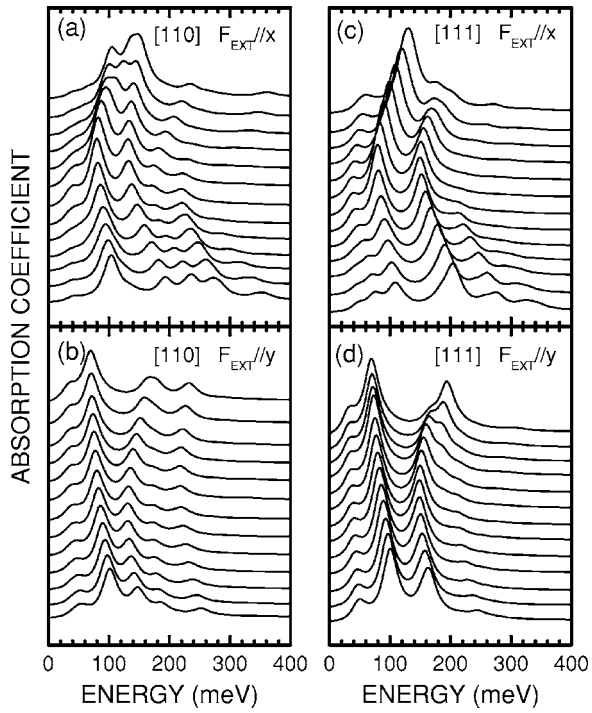

FIG. 12. Comparison of the intraband absorption coefficient of 10 nm wide hemispherical NC's with [110] (left column) and [111] (right column) crystalline orientations. F_{EXT} varies from −600 to 600 kV/cm from top to bottom pointing to x (top row) and y (bottom row) directions.

etry and the effective mass tensor plays a dramatic role in the NC optical properties through changes in the electronic structure and level degeneracy. Moreover, we found that F_{EXT}'s create additional peaks in the absorption spectra of large Si NC's that are not observed in small NC's. For non-spherical NC's, the response to F_{EXT} becomes highly anisotropic due to the interplay among NC shape, effective mass tensor, and its alignment with respect to the truncation. We remark that calculations performed in this work considered only one electron per energy valley. For higher NC occupation, we expect a much more complicated behavior, with absorption peaks and physical effects. Within the authors' knowledge, these effects have not been reported in the literature and are expected to stimulate experimental efforts in this direction. In order to observe the predicted effects it would be necessary to perform low energy spectroscopy in single (or few) NC's because random processes during NC formation may produce a large ensemble of NC's, and the fine structure of the absorption spectra of individual NC's might be smeared out by inhomogeneities of sizes and crystal orientations. The results presented in this work show that Si NC's with diameters of the order of 10 nm present good response to electric field intensities, which shows potential for real optoelectronic applications. As shown in Figs. 6–12, NC's with such dimensions are optically active in an energy range as large as 0.3 eV, which are suitable for IR detection in the 3–24 μm spectral range. Moreover, this energy range is also appealing for thermographic applications with detection capability over a very wide range of temperatures. These facts indicate that Si NC's might be alternative to the development of IP's that is compatible with standard Si technology.

ACKNOWLEDGMENTS

The authors would like to thank the Brazilian National Research Council (CNPq/CTENERG) for the financial support during the development of this work. This work was also supported by CNPq/CT-ENERG Grant No. 504330/2003-9.

[1] N. Tit and M. W. C. Dharma-Wardana, Solid State Commun. **106**, 121 (1998).
[2] N. Tit and M. W. C. Dharma-Wardana, Phys. Lett. A **254**, 233 (1999).
[3] D. J. Lockwood, *Semiconductors and Semimetals, Light Emission in Silicon: From Physics to Devices*, Vol. 49 (Academic Press, New York, 1998), and references therein.
[4] L. Pavesi, L. Dal Negro, C. Mazzoleni, G. Franzo, and F. Priolo, Nature (London) **408**, 440 (2000).
[5] A. Liu, R. Jones, L. Liao, D. Samara-Rublo, D. Rubin, O. Cohen, R. Nicolaescu, and M. Pannicia, Nature (London) **427**, 615 (2004).
[6] P. Boucaud, V. Le Thanh, S. Sauvage, D. Débarre, and D. Bouchier, Appl. Phys. Lett. **74**, 401 (1999).
[7] G. Allan and C. Delerue, Phys. Rev. B **66**, 233303 (2002).
[8] S. Tiwari, F. Rana, H. Hanafi, A. Hartstein, E. F. Crabbé, and K. Chan, Appl. Phys. Lett. **68**, 1377 (1996).
[9] A. Nakajima, T. Futatsugi, H. Nakao, T. Usuki, N. Horiguchi, and N. Yokoyama, J. Appl. Phys. **84**, 1316 (1998).
[10] G. Ledoux, O. Guillois, D. Porterat, and C. Reynaud, Phys. Rev. B **62**, 15942 (2000).
[11] J. S. de Sousa, J.-P. Leburton, A. V. Thean, V. N. Freire, and E. F. da Silva, Jr., Appl. Phys. Lett. **82**, 2685 (2003).
[12] See for example: Y. Ishikawa, N. Shibata, and S. Fukatsu, Thin Solid Films **321**, 234 (1998); J. A. Wahl, H. Silva, A. Gokirmak, A. Kumar, J. J. Welser, and S. Tiwari, IEDM **99**, 375 (1999); G. Ammendola, M. Vulpio, M. Bileci, N. Nastasi, C. Gerardi, G. Renna, I. Crupi, G. Nicotra, and S. Lombardo, J. Vac. Sci. Technol. B **20**, 2075 (2002); K. C. Scheer, R. A. Rao, R. Muralidhar, S. Bagchi, J. Conner, L. Lozano, C. Perez, M. Sadd, and B. E. White, Jr., J. Appl. Phys. **93**, 5637 (2003);
[13] A. Thean and J. -P. Leburton, J. Appl. Phys. **89**, 2808 (2001).
[14] S. L. Chuang, *Physics of Optoelectronic Devices—Wiley Series in Pure and Applied Optics*, Wiley, New York, 1995.
[15] Z. Bai, J. Demmel, J. Dongarra, A. Ruhe, and H. van der Vorst, *Templates for the Solution of Algebraic Eigen-value Problems: A Practical Guide* (SIAM, Philadelphia, 2000).
[16] L. N. Trefethen and D. Bau III, *Numerical Linear Algebra* (SIAM, Philadelphia, 1997).
[17] R. B. Lehoucq, D. C. Sorensen, and C. Yang, *ARPACK Users Guide: Solution of Large-Scale Eigenvalue Problems with Implicitly Restarted Arnoldi Methods* (SIAM, Philadelphia, 1998).
[18] L.-W. Wang and A. Zunger, J. Phys. Chem. **98**, 2158 (1994).